J Mater Sci (2012) 47:184–198
DOI 10.1007/s10853-011-5786-z

Interfacial heating during low-pressure cold-gas dynamic spraying of aluminum coatings

M. P. Dewar · A. G. McDonald · A. P. Gerlich

Received: 25 April 2011 / Accepted: 11 July 2011 / Published online: 26 July 2011

Abstract Low-pressure cold spraying was used to deposit aluminum particles ($\sim$25 μm diameter) on to low carbon steel, and the particle–particle interactions of the aluminum coating were analyzed. A simplified energy conservation model was developed to estimate the temperature at the interface of the deformed particle during deposition of the powder. The Johnson–Cook model was used to calculate the particle flow stress, which was used to estimate the total energy dissipated via plastic deformation during impact and spreading of the particle. Microstructural analysis was conducted to show that plastic deformation occurred mainly at the interfacial regions of the deformed particles. By coupling microstructural observations of the cold-sprayed particles with the energy conservation model, it was found that the interface between the aluminum particles contained recrystallized ultra-fine and nanocrystalline grain structures that were likely formed at temperatures above 260 °C, but the majority of particles likely achieved interfacial temperatures which were lower than the melting point of aluminum (660 °C). This suggests that local melting is not likely to dominate the inter-particle bonding mechanism, and the resulting interfacial regions contain ultra-fine grain structures, which significantly contribute to the coating hardness.

M. P. Dewar · A. P. Gerlich
Department of Chemical and Materials Engineering, University of Alberta, Edmonton, AB T6G 2V4, Canada

A. G. McDonald (✉)
Department of Mechanical Engineering, University of Alberta, Edmonton, AB T6G 2G8, Canada
e-mail: andre.mcdonald@ualberta.ca

List of symbols

A	Yield stress (MPa)
A_p	Projected area normal to gas flow (m^2)
A_s	Surface area of particle (m^2)
B	Johnson–Cook strain hardening constant (Pa)
Bi	Biot number
c_p	Specific heat capacity (J kg^{-1} K^{-1})
C	Johnson–Cook strain rate constant
C_D	Drag coefficient
d_p	Particle diameter (m)
d_{splat}	Splat diameter, after spreading (m)
D_{nozzle}	Nozzle diameter (m)
E_k	Kinetic energy (J)
E_p	Plastic deformation energy (J)
h	Heat transfer coefficient (W m^{-2} K^{-1})
k	Thermal conductivity (W m^{-1} K^{-1})
k_g	Thermal conductivity of free stream carrier gas (W m^{-1} K^{-1})
L_x	Distance traveled by particle (m)
m_p	Particle mass (kg)
M	Mach number
n	Hardening exponent
Nu	Nusselt number, $Nu = hd_p/k_g$
P_g	Absolute gas pressure (Pa)
Pr	Prandtl number, $Pr = c_p\mu/k_g$
r	Recovery factor
R	Gas constant (kJ kg^{-1} K^{-1})
Re_{d_p}	Reynolds number based on particle diameter, $Re_{d_p} = \rho_g(V_g - V_p)d_p/\mu_g$
t_c	Contact time (s)
t_i	Time at iteration i
t_x	Time traveled by particle (s)
T_{aw}	Adiabatic-wall temperature (K)
T_g	Free stream carrier gas temperature (K)

T_i	Temperature at increment i (K)
T_{initial}	Initial particle temperature prior to impact (K)
$T_{\text{interface}}$	Particle–substrate interface temperature (°C)
T_{bulk}	Temperature in the interior of the particle during deformation (°C)
T_{m}	Melting temperature (K)
T_{o}	Ambient temperature (K)
T_{sub}	Temperature of substrate (K)
V_{g}	Carrier gas velocity (m/s)
V_i	Particle velocity at increment i
V_{p}	Particle velocity (m/s)
X	Nozzle length (m)

Greek symbols

α	Thermal diffusivity (m^2s^{-1})
γ	Specific heat ratio
δ	Lamellae thickness (m)
ε_{f}	Final von Mises equivalent strain
ε_{i}	Equivalent strain at increment i
ε_i*	Strain rate at increment i
θ	Non-dimensional interface temperature
μ_{g}	Viscosity of free stream carrier gas (kg m^{-1} s^{-1})
μ_{s}	Viscosity of gas at particle surface (kg m^{-1} s^{-1})
μ_{o}	Reference viscosity of gas (kg m^{-1} s^{-1})
ξ	Non-dimensional particle diameter
ρ	Particle/splat density (kg m^{-3})
ρ_{g}	Gas density (kg m^{-3})
σ	Von Mises equivalent flow stress (Pa)
Ω	Particle volume (m^3)
Ω_{splat}	Volume of a particle after impact and deformation on the substrate (m^3)

Introduction

Cold-gas dynamic spraying ("cold spraying") is a process in which small, unmelted metal or alloy powder particles (1–100 μm in diameter) are accelerated to supersonic speeds (500–1200 m/s) to form a dense protective coating. Due to the exceptionally high kinetic energies of the particles in flight [1], high strain rates will occur during impact [2]. Similar to ballistic impacts, cold-sprayed particles will also experience hardening and heat generation during impact and spreading [3]. It has been recognized that when this localized heating occurs, there is a high probability of melting at the particle–substrate interface during deposition of low melting point alloys due to the high kinetic energies produced [4–6]. Grujicic et al. [4] and Assadi et al. [5] have proposed that the bonding occurs either by mechanical interlocking from high impacting pressures and temperatures or by adiabatic shear instabilities, which cause localized heating at the particle–substrate interface. The microstructures may be highly inhomogeneous, with some nearly spherical particles and others, which are substantially deformed. Though it has been suggested that the presence of spherical particles observed at the interface after coating removal signals the formation of liquid at the interface, the mechanism for this and how it relates to melting is not clearly understood [7].

It has been argued that melting plays an important role in the formation of thin jets of material at the interface during high pressure cold spraying at particle velocities greater than 700 m/s [8–11], however, debate remains over whether melting occurs at the interface during low-pressure cold spraying since the microstructures are so inhomogeneous. No direct temperature measurements during cold spraying have been performed to confirm the melting temperature is achieved, and it is difficult to define what would constitute microstructural evidence of melting in the case of the cold spray process. These aspects make it challenging to quantify the contributions of metallurgical and mechanical interlocking to the inter-particle bonding mechanism [12]. However, based on the observations of the tensile yield strength and fracture of free-standing sheets of cold-sprayed material, it appears that metallurgical bonding occurs at limited regions between the splat interfaces [2].

Regardless of whether localized melting at the interface dominates during the process, adhesion of the particles to the substrate in cold spraying is promoted when the oxide layer at the particle surface is broken down and metallurgical bonding is established between the particle and the substrate. It has been shown that successful bonding of the particles is achieved above a critical in-flight particle velocity, which may be comparable to the velocity required for adiabatic shear instability [2]. These adiabatic shear instabilities may produce sufficient heat for melting to occur at the splat–substrate interface [2, 13, 14]. Though some studies have been conducted, the exact criteria for producing adiabatic shear instabilities for a given set of spraying parameters is still not well understood. It has been shown that formation of the shear instabilities is dependent on the particle's velocity and size, whereas the extent of these instabilities is governed by an interaction between the kinetic energy gained by the particle, the material's flow strength, and heat generated by the particle during plastic deformation [2, 13].

Formation of shear instabilities depends on a balance between strain hardening and thermal softening of the material during deformation of the particle [4]. If thermal softening dominates over strain hardening and strain rate hardening, the material of the impacting particle displays viscous-like behavior leading to the formation of jets similar to those found in explosion welding [15]. Otherwise, if strain hardening dominates over thermal softening, inadequate heat, and deformation are generated at the

interface and it is unlikely that the particle will adhere to the surface. It has been argued that these turbulent jets remove oxides or contaminants found at the interface to form a metallurgical bond between the impacting particle and the substrate. The dynamic recrystallization in shear bands also shows evidence of localized deformation at the particle–substrate interface where a sufficient amount of thermal energy can be generated for metallurgical bonding [16, 17]. Many have suggested that the heat due to plastic deformation in this localized region is sufficient to produce melting only at these interfacial regions [18], since kinetic energy at the critical particle velocity for adhesion is clearly below that required to melt the entire particle [13].

Since there are extreme conditions of temperature and strain rate occurring between particles during cold spray impact, the deformation mechanisms in these interfacial regions will play a major role in the final microstructure and properties of the coating. The dynamic recrystallization produced by strains in the localized regions at the particle–substrate interface may result in extensive grain refinement, allowing nanocrystalline grain structures to be produced in the final deposit [19]. Nanocrystalline materials exhibit high hardness and yield strength due to the large fraction of grain boundaries in the material, and this Hall–Petch effect has been studied in nanocrystalline materials, and is particularly significant at grain sizes less than 100 nm [20]. Studies conducted by Hall et al. [19] and Ajdelsztajn et al. [21] have shown that nanocrystalline powders can be consolidated during impacts in the cold spray process. Due to the short residence time in the nozzle, the particles are not significantly heated during spraying. As a result, grain coarsening is suppressed during cold spraying, unlike the case of air plasma or high-velocity oxy-fuel spraying where particles are completely or partially melted.

Rather than completely melting the particles with a high-temperature flame or plasma, the majority of heat at the particle impact point during cold spraying is generated by plastic deformation that occurs over a very short time period. Under these conditions, the stress–strain behavior of a material can be considered to be adiabatic [4]. During impact, where substrate heating occurs due to the deformation of the particle, thermal softening also occurs, which significantly lowers the flow stress of the material. It has been argued that the minimum particle velocity needed to promote adhesion of a particle is determined by the ability to promote adiabatic shear instability [22]. Some recent work has shown that these interfacial regions contain fine recrystallized grains [16, 17] which exhibit higher hardness [23]. However, no quantitative correlation has been made between the plastic energy dissipated, the dimensions of the fine-grained interfacial regions, and the temperatures which can be achieved at the impacting interface.

This study examines the heat generation and deformation mechanisms during low-pressure cold-gas dynamic spraying of commercially pure aluminum powder. A combination of optical and transmission electron microscopy (TEM) was used to study the deformation imposed in the particles, and existing models for compressible fluid flow, material deformation, and heat transfer were applied to investigate the role of localized heating and estimate the temperatures at the contact interface. The focus of this study is to show how these relate to the microstructures and particle bonding mechanisms produced in the final deposit.

Experimental method

Spheroidal, gas atomized aluminum powder (54NS-1, Sulzer Metco, Westbury, NY, USA) was used for this study. The composition of the powder is shown in Table 1, which corresponds to commercially pure aluminum alloy of grade AA 1080. The powder was sieved (RX-29-CAN, W.S. Tyler, Mentor, OH, USA) to obtain a particle size distribution lower than 38 μm (−38 μm).

To fabricate the coatings, the aluminum powder was deposited on a low carbon steel substrate using a low-pressure cold-gas dynamic spraying system (Model SSM P3800-001, Centerline SST, Windsor, ON, Canada). In all the deposits, compressed air was used as the carrier gas, and the gas pressure and temperature were fixed at 90 psig (620 kPa gage) and 375 °C, respectively. The converging–diverging de Laval nozzle in the cold spray torch was 140 mm long, had a throat diameter of 2.54 mm, and an exit diameter of 6 mm. During spraying, the cold spray nozzle was operated by a robot (Motoman-HP20, Yaskawa Electric Corporation, Waukegan, IL, USA). The stand-off distance, the distance between the nozzle and the substrate, was 10 mm and the transverse speed was 10 mm/s. A DPV-2000 in-flight particle diagnostic tool (Tecnar Automation Ltée, St-Bruno, QC, Canada) was used to measure the average diameter and velocity of the aluminum particles immediately before impact on the substrate. Prior to deposition, the substrates were roughened by grit-blasting with #24 grit alumina.

Samples for optical microscopy imaging were prepared by first mounting and mechanically grinding the samples with silicon carbide (SiC) abrasive from 320 to 1200 grit, followed by diamond polishing with 1 μm particles. They were electropolished with an aluminum cathode and a

Table 1 Composition of the aluminum particles (wt%)

Al	Cu	Fe + Si	Mn	Zn	Others
99.79	0.01	0.15	0.01	0.01	0.04

solution of 25 vol.% nitric acid (HNO_3) and 75 vol.% methanol at a temperature of 30 °C and a voltage of 12 V for 1 min. Particle splats and grain boundaries were revealed by electrolytically etching the coating using a 3 vol.% solution of fluoroboric (HBF_4) acid at room temperature and 20 V for 60–90 s.

Microhardness indentations were made on mounted and polished coating samples using a microhardness indenter (MVK-H1, Mitutoyo, Aurora, IL, USA) with a 10 g indenter load and a dwell time of 15 s. Microhardness values are reported as an average of five measurements in this study ($n = 5$).

Transmission electron microscopy samples were prepared from 3 mm disks removed from the transverse direction of the coating with a low-speed diamond saw, and were thinned with a twinjet electropolisher using the same conditions as those used for the optical samples. The TEM samples were examined using a microscope (Model 2010, JEOL, Peabody, MA, USA) operating at 200 kV. Microstructures observed in the optical and TEM micrographs were analyzed using Adobe Photoshop CS3, where 130 individual particle splats were analyzed for their circularity, width, height, and area.

Mathematical models

Particle–substrate interfacial temperature

The law of conservation of energy was used to estimate the particle–substrate interface temperature. In this study, only the coating material was considered and hence, the previously deposited layer of the coating was regarded as the substrate from this point onwards. It was assumed that the kinetic energy of the in-flight particle was converted to plastic deformation energy and heat. The heat generated occurred primarily at the interface, and is the difference between the original kinetic energy of the particle and the plastic deformation energy. It is defined as,

$$E_{\mathrm{k}} - E_{\mathrm{p}} = \rho \frac{\pi d_{\mathrm{splat}}^2 \delta}{4} c_p (T_{\mathrm{interface}} - T_{\mathrm{initial}}). \quad (1)$$

The $\frac{\pi d_{\mathrm{splat}}^2 \delta}{4}$ term is the volume of the interface through which conduction and thermal softening has occurred. This thin interface between each of the particles can be described as a lamella with a thickness, δ, which defines the region over which the localized heating has occurred, and can be estimated through analysis of the coating microstructure. The measurement of the average thickness δ was conducted using both optical microscopy on samples that were etched, and with TEM observations. Examples are shown in the micrographs, and measurements were all taken perpendicular to the direction of the lamella with the dimensions of δ indicated, where applicable. It was observed that etching using 3% fluoroboric solution preferentially attacks these lamellae at the interfaces of the particles, and the optical measurements of the etched regions are consistent with the thickness of the deformed bands of material observed by TEM (as shown in later figures).

The lamella thickness will correspond to the locations of localized and inhomogeneous deformation in the splat [7, 17, 24]. The term on the right-hand side of Eq. 1 represents the heat that is generated at the interface to increase the temperature from an initial value, T_{initial}, to the interfacial temperature, $T_{\mathrm{interface}}$. From the perspective of heat transfer analysis, the interface temperature that will result from Eq. 1 will be a conservative upper-limit approximation since it is assumed that none of the kinetic energy that is converted to heat is lost to the environment, to the rest of the bulk splat, or to the substrate. All the physical and thermal properties of the splat material were assumed to be constant.

Plastic deformation of the particle during cold spraying will generate significant stress and strain. The plastic deformation energy (E_{p}) can be determined by calculating the area under the stress–strain curve, given by

$$E_{\mathrm{p}} = \Omega \int_0^{\varepsilon} \sigma[\varepsilon(t)]\mathrm{d}\varepsilon = \Omega \sum_{i=1}^{n} \sigma(\varepsilon_i)\Delta\varepsilon. \quad (2)$$

A stress–strain curve for a given particle size was developed by assuming a one-dimensional plastic deformation model, and the area under the curve was estimated by using Riemann sums and iteration. One hundred iterations were done in increments by determining a time step ratio, t/t_{c}, where the total contact time, t_{c}, was determined as the particle–substrate interaction time over which the particle spreads, strain hardens, and generates heat. t_{c} was calculated by dividing the total displacement of the particle, or the difference in the height of the particle before and after impact, by the mean velocity experienced by the particle during spreading. The mean velocity accounts for the deceleration of the particle during impact, in which a linear decrease in speed was assumed [5].

Flow stress is not constant during deformation of an impacting particle, and it depends on the strain, strain rate, and temperature. During adiabatic heating, an iterative process may be used to determine the flow stress of the particle interface at each time step during plastic deformation. The energy dissipated via plastic deformation must be taken into account as this will induce heating and thermal softening of the material. It has been shown that at high strain rates, the fraction of energy dissipated as heat during plastic deformation increases and approaches 100%

[25]. For the purposes of estimating the flow stress, it was assumed that the heat energy during plastic deformation was uniformly distributed through the bulk volume of the deforming particle, resulting in a bulk temperature increase to T_{bulk} within the particle. The flow stress of aluminum particles during impact was estimated by using the Johnson–Cook plasticity model, expressed as [26]:

$$\sigma = [A + B\varepsilon^n][1 + C\ln(\varepsilon^*)]\left[1 - \frac{T_{\text{bulk}} - T_{\text{initial}}}{T_{\text{m}} - T_{\text{initial}}}\right], \tag{3}$$

where the final von Mises equivalent strain (ε_{f}) can be determined by the equation,

$$\varepsilon_{\text{f}} = \frac{\sqrt{2}}{2}[(\varepsilon_1 - \varepsilon_2)^2 + (\varepsilon_2 - \varepsilon_3)^2 + (\varepsilon_3 - \varepsilon_1)^2]^{1/2}. \tag{4}$$

The values for the total strains ε_1 and ε_2 can be estimated from optical micrographs of the etched coating by examining the geometry of splats in the x- and y-coordinates, respectively, and by assuming that the initial particles had a spherical shape. The remaining strain value, ε_3, is the true strain in the z-coordinate, which is determined by considering conservation of mass after the ε_1 and ε_2 strains are determined from cross-sectional micrographs.

The flow stress of the particle was calculated in an iterative manner, using the Johnson–Cook model to estimate the rate of thermal softening, and taking into account the adiabatic heating of the particle to a bulk temperature (T_{bulk}) at each iteration based on the plastic deformation energy given by Eq. 2. At each iteration, a new particle velocity, strain, and strain rate was calculated for subsequent intervals. This is important as the particle will decelerate with each time interval and the kinetic energy of the particle will be gradually converted to heat resulting from the plastic deformation. Previous modeling studies have shown the velocity at the trailing edge of the particle to decrease linearly with time during impact [5, 22] as:

$$V_i\left(\frac{t_i}{t_{\text{c}}}\right) = V_{\text{p}}\left(1 - \frac{t_i}{t_{\text{c}}}\right). \tag{5}$$

Therefore, the strain can be calculated as:

$$\varepsilon_i\left(\frac{t_i}{t_{\text{c}}}\right) = \varepsilon_{\text{f}}\frac{t_i}{t_{\text{c}}}\left(2 - \frac{t_i}{t_{\text{c}}}\right). \tag{6}$$

It has been shown that the strain decreases linearly during impact for the bulk of the particle as per Eq. 6 [4], although more complex modeling studies have shown that for certain particle impact velocities. When velocities are sufficient, a plastic to viscous transition region may occur in a thin layer of material at the interfacial regions during impact [4, 5]. In the case of the flow stress model, only deformation in the bulk of the particle is considered, and material at the interfacial regions will be discussed later. Finally, the strain rate is calculated using a forward difference method, where

$$\varepsilon_i* = \frac{\varepsilon_{i+1} - \varepsilon_i}{t_{i+1} - t_i}. \tag{7}$$

If the initial condition (at $t = 0$) of the one-dimensional model is taken to be the instant immediately before the particle contacts the substrate surface, Eq. 5–7 can be solved for each time interval until the total contact time has been reached and a maximum interfacial temperature has been achieved. The bulk particle temperature at each interval during impact is used to determine the degree of thermal softening resulting from the plastic deformation energy in Eq. 2, assuming adiabatic conditions prevail and that all of the energy is transferred into heat.

In this study, 160 intervals were chosen to represent the stress–strain curves during impact of the particles. Since no stress, strain, temperature, or microstructural gradients are considered in the flow stress model, the values obtained are, effectively, only an average of the bulk values. If the total plastic energy dissipated during plastic deformation, according to Eq. 2, is substantially less than the kinetic energy available, then it is likely that shear localization at the particle interface will occur and cause the interfacial temperature to increase above the bulk particle temperature. This surplus of kinetic energy may be sufficient to promote local melting [27]. Before the flow stress can be estimated, the velocity and temperature of the particle when it makes initial contact with the substrate must be measured or estimated analytically as shown in the following sections.

Particle-gas heat transfer

Equation 1 shows that the temperature of the in-flight particle (T_{initial}) prior to impact will be needed in order to estimate the interfacial temperature ($T_{\text{interface}}$) between the aluminum splats and the substrate surface. The particles were heated by the hot compressed air through forced convective heat transfer. Neglecting radiation effects, a lumped capacitance model was developed by assuming that the Biot number (Bi) was much less than 0.1, which is a requirement for validity of the lumped capacitance model. The Biot number is the ratio of internal conduction and external convective resistances to heat transfer, and for a sphere, it is given as.

$$Bi = \frac{hd_{\text{p}}}{6k}. \tag{8}$$

The assumption of a small Bi is probably valid for the in-flight aluminum particles. For particle diameters on the order of 50×10^{-6} m and aluminum thermal conductivity of approximately 200 W/m K, the Biot number will probably be much smaller than 0.1.

The particle temperature that is derived from the lumped capacitance model will vary only with time. The temperature of the particle prior to impact will be governed by the law of conservation of energy. The equation used in this study is modified from that derived by Jiji [28] to include the adiabatic-wall temperature (T_{aw}) as

$$T(t) = T_{aw} - (T_{aw} - T_o)\exp\left[-\frac{hA_s}{\rho c_p \Omega}t\right]. \quad (9)$$

Heat will be added to the particle as it traverses the total length of the nozzle and stand-off distance. The in-flight time, $t_x = \frac{L_x}{V_p}$, will be used to approximate the initial temperature ($T_{initial}$) of the particle immediately prior to impact on the substrate:

$$T_{initial} = T_{aw} - (T_{aw} - T_o)\exp\left[-\frac{hA_s}{\rho c_p \Omega}\frac{L_x}{V_p}\right]. \quad (10)$$

The temperature, T_o, is the powder particle temperature before it entered the cold spray nozzle, which was assumed to be that of the ambient at 25 °C.

As the particles move through the compressed gas, the solid surface will be heated by the hot gas and fluid viscous shear work. Heat will be conducted away from the surface into the particle, reducing the amount of energy available to induce a surface temperature rise. When this effect has been considered, the equilibrium temperature of the surface or the adiabatic-wall temperature, T_{aw}, will be lower than the total temperature of the fluid. A recovery factor, r, is used to determine the value of the adiabatic-wall temperature relative to the average temperature of the free stream carrier gas, T_g. Shapiro [29] has defined the adiabatic-wall temperature as

$$T_{aw} = \left[1 + r\frac{(\gamma - 1)}{2}M^2\right]T_g. \quad (11)$$

Theoretical analyses and experimentation have been used to generate a simple result for the recovery factors for supersonic air flow over a variety of geometrical shapes as [30]

$$r \approx \sqrt{Pr}. \quad (12)$$

For all the geometrical shapes studied in the experiments, the Reynolds number of the flow was less than 5×10^6. The forced convective heat transfer coefficient, h, can be determined by using the theory of cones for laminar, supersonic air flow over a body of revolution [31], which is defined as

$$h \approx 0.50\frac{k_g}{d_p}\sqrt{Re_{d_p}}, \quad (13)$$

where the thermal properties should be taken at the free stream gas temperature (T_g).

The use of Eqs. 12 and 13 assumes that the compressed air flow in the cold spray nozzle will be supersonic and the flow will be laminar over the spherical particles. Values of the Mach and Reynolds numbers will be verified in this study.

Gas flow

The Reynolds number for flow over the in-flight particle is required to determine the heat transfer coefficient shown Eq. 13. The aluminum particles are accelerated to velocities of 500 to 1000 m/s in a supersonic compressed gas jet. Under these conditions, the Reynolds number is

$$Re_{d_p} = \frac{\rho_g(V_g - V_p)d_p}{\mu_g}. \quad (14)$$

The gas velocity, V_g, can be calculated by using the mathematical definition of the speed of sound,

$$V_g = M\sqrt{\gamma RT_g}. \quad (15)$$

The gas density, ρ_g, was determined by using the ideal gas relationship, $\rho_g = \frac{P_g}{RT_g}$, under the assumption that the heated air was an ideal gas. With the definition of the gas velocity and density, the Reynolds number becomes

$$Re_{d_p} = \frac{P_g(M\sqrt{\gamma RT_g} - V_p)d_p}{\mu_g RT_g}. \quad (16)$$

The Mach number of the compressed gas jet is the only unknown parameter on the right-hand side of Eq. 16. A force balance over the particle could be conducted to develop a strategy to estimate the gas Mach number. Acceleration of the compressed gas is achieved through a converging–diverging de Laval type nozzle in the cold spray torch, where the acceleration of the particle is related to the drag force through [32]:

$$m_p\frac{dV_p}{dt} = m_p V_p\frac{dV_p}{dx} = \frac{C_D A_p \rho_g (V_g - V_p)^2}{2}. \quad (17)$$

In Eq. 17, it was assumed that the particle concentration in the gas flow is low, such that particle–particle interactions can be neglected. The gas flow, with respect to the nozzle wall, is adiabatic and frictionless. Furthermore, it was assumed that the particle is only accelerated by the gas drag force. Assuming that the gas in the de Laval nozzle was flowing at a constant velocity, and neglecting any temperature or pressure gradients, Eq. 17 was integrated to give [32]:

$$\log\left(\frac{V_g - V_p}{V_g}\right) + \frac{V_g}{V_g - V_p} - 1 = \frac{C_D A_p \rho_g x}{2m_p}. \quad (18)$$

For supersonic flow, where the Mach number is greater than 1, the drag coefficient (C_D) ranges between 0.8 and 1.0

[29]. For a given particle with diameter and in-flight velocity measured by the DPV-2000, an initial estimate of the value of the drag coefficient between 0.8 and 1.0 can be used to estimate the gas velocity from Eq. 18. With the gas velocity known, the Mach number can be determined from Eq. 15. The Mach number determined from Eq. 15 will be compared that obtained from the C_D versus M chart presented by Shapiro [29]. Additional estimates of the value of the drag coefficient will be applied in an iterative process, involving Eqs. 15 and 18 until convergence of the Mach numbers occurs to within one decimal place. Variations in the gas velocity will occur in the cold spray nozzle and will cause variations in the Mach number and C_D. However, the errors induced in the heat transfer model and temperature estimates by these variations will probably be small. This is due to the narrow range of C_D for Mach number greater than 1, where variations in Mach number will produce variations in C_D between 0.8 and 1 [29]. For Mach numbers greater than 1.5, the variation in C_D is reduced further to approximately 0.92 and 1.

Estimation of particle interface temperature

The interface temperature between the splat and the substrate is found after rearrangement of Eq. 1 to give

$$T_{\text{interface}} = \frac{4(E_k - E_p)}{\rho\pi d_{\text{splat}}^2 \delta c_p} + T_{\text{initial}}. \quad (19)$$

The diameter of the splat (d_{splat}) and the thickness of the interfacial region (δ) that is subject to localized heating will be estimated after analysis of the microstructure of the coating and splats. Coating fabrication requires the deposition of in-flight particles on to previously deposited particles and splats. The previously deposited splats will become the substrate for the subsequent in-flight particles. The temperature in the interfacial regions between the splats will be higher than that of the rest of the bulk splat and the substrate during impact and after spreading. If the thickness of the interfacial regions are also much smaller than the total thickness of the deformed splat and substrate, from the perspective of heat transfer over the small time scales expected in this problem, the splat and substrate can be assumed to be semi-infinite media relative to the localized interfacial regions. In this case, heat conducted from the interface into the rest of the splat and substrate will be low during the spreading process, which justifies the assumption that all the heat generated from the difference between the in-flight particle kinetic energy and energy dissipated via plastic deformation is localized in the interface volume between the splats. The determination of the heat dissipated away from the interface would require more complex diffusive heat conduction analyses. However, Assadi et al. [5] has cautioned that, based on the small particle diameters encountered in cold spraying applications, the heat conducted from the interface would be lower than that predicted by the diffusive heat equation.

Results and discussion

In-flight particle velocities and temperature

The interface temperature between the splat and the substrate in low-pressure cold spraying will determine the resulting microstructures and the feasibility of local melting during the process. The energy balance presented in Eq. 1 to determine the interface temperature depends on knowledge of the in-flight particle velocity to calculate the kinetic energy of the particles. Data gathered from the DPV-2000 showed that the average diameter of the aluminum particles was 25 ± 8 μm and the average particle velocity was 517 ± 42 m/s ($n = 19$). The standard deviations and the number of samples are presented with each average. Based on these measurements, an iterative process involving Eqs. 15 and 18 and the C_D versus Mach number chart for flow over spheres [29] was used to estimate the Mach number and C_D value for the compressed air and spherical particles, respectively. The Mach number was approximately 1.1 and the C_D value was approximately 0.84. The free stream gas velocity was determined to be approximately 570 m/s by using Eq. 15. Air properties were taken at 400 °C. Table 2 presents Reynolds number estimates using the average particle diameter and velocity measured with the DPV-2000 diagnostic tool. Table 2 also includes data based on one standard deviation from the mean of the particle diameters and velocities in order to include variation in particle size and velocity found throughout the gas stream. Further, given that the Reynolds numbers are on the order of 10^2, laminar flow over the

Table 2 Particle velocities and Reynolds numbers

d_p[a] (μm)	Re_{d_p}	V_p[a] (m/s)	A_p (m^2)	Ω (m^3)
17	113	475	2.3×10^{-10}	2.6×10^{-15}
17	122	517	2.3×10^{-10}	2.6×10^{-15}
17	132	559	2.3×10^{-10}	2.6×10^{-15}
25	236	475	4.9×10^{-10}	8.2×10^{-15}
25	257	517	4.9×10^{-10}	8.2×10^{-15}
25	278	559	4.9×10^{-10}	8.2×10^{-15}
33	401	475	8.6×10^{-10}	1.9×10^{-14}
33	436	517	8.6×10^{-10}	1.9×10^{-14}
33	472	559	8.6×10^{-10}	1.9×10^{-14}

[a] Values of the particle diameter and velocity are the average values of ±1 standard deviation at 25 ± 8 μm and 517 ± 42 m/s, respectively

entire particle can be assumed. Legoux et al. [33] found similar velocities for aluminum particles injected into compressed nitrogen at 400 °C and 90 psig (620 kPa gage) in a low-pressure cold spray system similar to that used in this study. They used the DPV-2000 in-flight particle diagnostic tool and found that under these conditions, aluminum particles with diameters of 36 μm will have an in-flight velocity of 568 m/s. Given that nitrogen and air have approximately similar properties, the velocity measured by Legoux et al. [33] supports those presented in Table 2.

The in-flight temperature of the particles immediately prior to impact ($T_{initial}$) was determined by using Eqs. 10–12, and data from Table 2. Table 3 shows that the initial temperatures of the 17, 25, and 33 μm particles before impact, ranged from 160 to 273 °C, over the range of particle velocities (475–559 m/s). These values correlate well with previous results showing that particle in-flight temperatures in cold spraying are typically on the order of 10^2 °C [19]. Values of the heat transfer coefficient (h) are also presented in Table 3. The large values of the heat transfer coefficient (order of 15×10^3 W/m^2 °C) support an initial assumption that heat transfer to the spherical particles occurs by forced convection. The Biot number was found to be much less than 0.1 (see Table 3), confirming the validity of the lumped capacitance model and the assumption of uniform temperature (no spatial variation) throughout the particles in flight.

Adiabatic heating due to bulk deformation

Equation 1, coupled with the Johnson–Cook plasticity model, was used to estimate the energy dissipated during plastic deformation, E_p. The Johnson–Cook constants for 1080 Al alloy (99.8 wt% Al) are not available. However, Akarca et al. [34] have determined the constitutive parameters for commercially pure 1100 Al alloy (99.0 wt% Al). Based on room temperature mechanical testing data, the yield and tensile strengths for 99.8% pure aluminum are both approximately 33% lower than that of 99.0% pure aluminum [35]. Therefore, the A and B parameters in the Johnson–Cook equation for a 1080 Alloy were adjusted to reflect this decrease in the strength values with higher purity, while all the other constants were assumed to remain unchanged from those of the 1100 Al alloy. These parameters are listed in Table 4, and will be used to generate the flow stress and strain relation of the deforming cold-sprayed particles.

The cross-section of the cold-sprayed aluminum coating is shown in Fig. 1, with some of the individual particles highlighted as examples, ranging in width from 58 to 71 μm. The morphology of the splats can clearly be distinguished in the larger particles, which exhibit only small changes in their aspect ratio, while smaller particles appear to have been more severely deformed and elongated. The average strains were calculated from the micrographs by taking the average height and width of the larger particle splats, and comparing these values to the volume of an ellipsoid with the same corresponding major and minor axis dimensions. The through-thickness dimension of a splat was assumed to be equivalent to the observed width and conservation of volume, $\Omega_{particle} = \Omega_{splat}$, allowed correlation of the observed strains to an initial particle diameter. Based on measurements, for the particles with initial diameters of 17, 25, and 33 μm, the average final diameter of the splats, d_{splat}, was 28, 41, and 54 μm, respectively. From the measured values of ε_1 and ε_3, the final von Mises equivalent strain for these particles was determined using Eq. 4 to be $\varepsilon_f = 1.25 \pm 0.37$ ($n = 105$).

Table 3 Particle heat transfer data and in-flight temperature

d_p (μm)	V_p (m/s)	h (W/m^2 °C)	Bi	$T_{initial}$ (°C)
17	475	14,759	1.8×10^{-4}	273
17	517	15,398	1.8×10^{-4}	265
17	559	16,011	1.9×10^{-4}	259
25	475	14,536	2.6×10^{-4}	208
25	517	15,165	2.7×10^{-4}	202
25	559	15,769	2.8×10^{-4}	197
33	475	14,358	3.3×10^{-4}	170
33	517	14,978	3.5×10^{-4}	165
33	559	15,576	3.6×10^{-4}	160

Table 4 Johnson–Cook parameters for 1100 aluminum alloy

Parameter	A (MPa)	B (MPa)	n	C
value	105	57	0.65	0.013

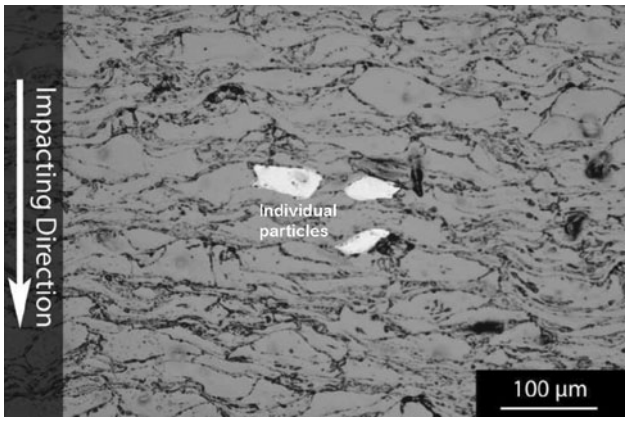

Fig. 1 Optical micrograph of the cold-sprayed aluminum coating

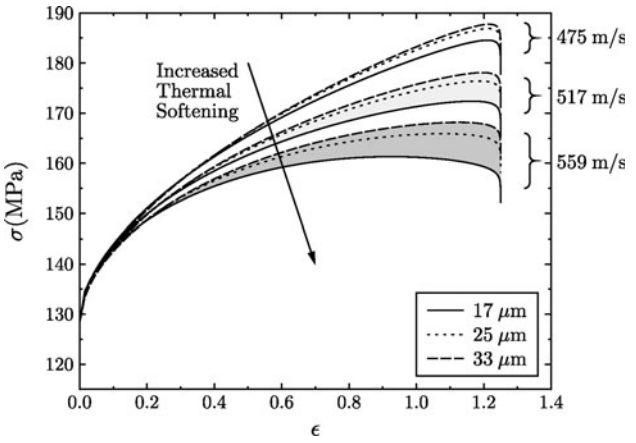

Fig. 2 Stress–strain relationships calculated from the Johnson–Cook model for different particle diameters

A wide distribution of splats was observed, with a small number that underwent very little deformation retaining circularity close to 1, and a large portion that experienced extreme amounts of deformation having circularities as low as 0.15. Particles that experienced little deformation were probably larger than 38 μm given some larger particles could have remained in the stock powder sample after sieving. It should also be noted that the particle splats shown in Fig. 1 have experienced impacts from subsequent particles. Therefore, the final von Mises equivalent strain of $\varepsilon_f = 1.25$ should be considered as an upper limit, and would be lower when describing a single particle impact on the surface.

The stress–strain (σ–ε) curves for the various diameters and velocities of the aluminum particles are shown in Fig. 2. The results suggest that the particles exhibit greater thermal softening as the particle diameter decreases, while localization behavior in the aluminum particles is more prominent for the particles with higher velocities. Particle size variation also appears to have a more pronounced effect as particle velocity increases, shown by the shaded areas of Fig. 2. For the particles achieving higher velocities in the jet stream, more of the kinetic energy gained during flight can be converted into heat in the localized region, while a wider distribution of interfacial temperatures will be observed, depending on the particle size. The energy that is converted to heat in the localized region is obtained, in part, from the total energy dissipated via plastic deformation in the σ-ε curves in Fig. 2. Table 5 lists the kinetic and plastic deformation energies, as well as the energy difference ($E_k - E_p$) that was converted to heat at the interface. Since E_p is a function of σ, ε, and d_p, the velocity will not have an effect on the plastic deformation energy of the particles, and will only serve to determine the amount of kinetic energy gained before impact. Uniform volumetric heating was assumed in order to calculate the bulk temperature, which was applied over the entire volume of the particle that was deformed from a spherical to ellipsoidal shape. However, the calculation of $T_{interface}$ from Eq. 19 requires knowledge of the effective interface thickness (δ), which determines the volume over which the difference between the kinetic and bulk particle deformation energies ($E_k - E_p$) was dissipated during impact. The dimensions of δ can be determined by comparing the recrystallized grain structures in the original powder base material versus those at the particle interfaces, and this is measured by optical microscopy after etching, as well as by TEM.

Coating microstructure and hardness

Figure 3 shows the coating microstructure following electrolytic etching, revealing coarse equiaxed grains within the bulk of the splats. In the thin lamellae at the splat boundaries, it was confirmed by TEM that this material contains fine recrystallized grains which are much finer than the bulk of the particle or the initial powder (as shown in subsequent TEM micrographs). The observations indicate that much higher strains occurred in the lamellae at the localized regions at the splat boundaries, resulting in recrystallization and grain refinement. The coarse-grained regions within the interior of the splats had an average grain size of 6.5 ± 1.8 μm ($n = 30$). The microstructure of

Table 5 Kinetic energy, energy dissipated via plastic deformation, and maximum interface temperatures of the aluminum particles

d_p (μm)	V_p (m/s)	E_k (J)	E_p (J)	$E_k - E_p$ (J)	T_{bulk} (°C)	$T_{interface}$ (°C)
17	475	7.9×10^{-7}	5.4×10^{-7}	2.5×10^{-7}	312	402
17	517	9.3×10^{-7}	5.2×10^{-7}	4.1×10^{-7}	331	480
17	559	1.1×10^{-6}	5.0×10^{-7}	5.9×10^{-7}	352	566
25	475	2.5×10^{-6}	1.7×10^{-6}	7.8×10^{-7}	247	397
25	517	3.0×10^{-6}	1.7×10^{-6}	1.3×10^{-6}	267	514
25	559	3.5×10^{-6}	1.6×10^{-6}	1.8×10^{-6}	289	643
33	475	5.8×10^{-6}	4.0×10^{-6}	1.8×10^{-6}	209	418
33	517	6.8×10^{-6}	3.9×10^{-6}	3.0×10^{-6}	229	575
33	559	8.0×10^{-6}	3.8×10^{-6}	4.2×10^{-6}	252	745

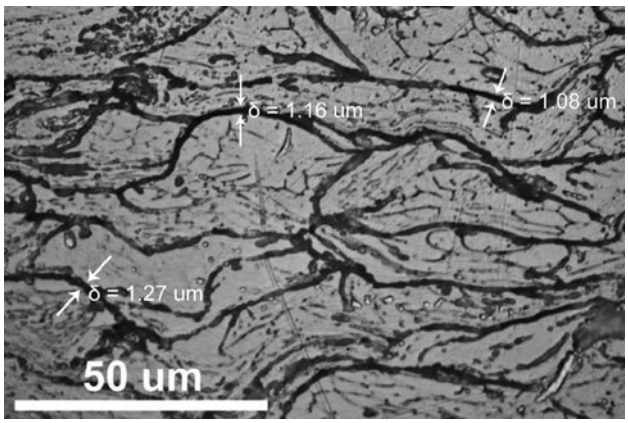

Fig. 3 Optical micrograph of the electrolytically etched aluminum cold-sprayed coating

a typical as-received powder particle shown in Fig. 4 had an average grain size of 13.4 μm ($n = 134$). The average thickness of the lamellae, δ, was measured to be 1.2 ± 0.4 μm ($n = 47$) in the through-thickness direction of the coating, with submicron grains occurring within these lamellae. The reduction in grain size between the as-received powder particle and that of the interior of the splats suggests that deformation and recrystallization occurred in the interior of the splat. However, the drastic reduction of grain size in the lamellae regions, close to the splat boundaries, suggests that far more significant deformation occurred in these lamellae.

The as-received powder had a Vickers hardness of 33 ± 2.2 HV ($n = 5$). Although only the indents in the centers of the particles were considered, it should be noted that with a 10 g load this value may be slightly overestimated due to plastic zone edge effects. Microhardness indents and results on the deposited aluminum coating are shown in Fig. 5, where coarse-grained regions of the splats had average hardness values of 42 ± 5.2 HV ($n = 5$), and

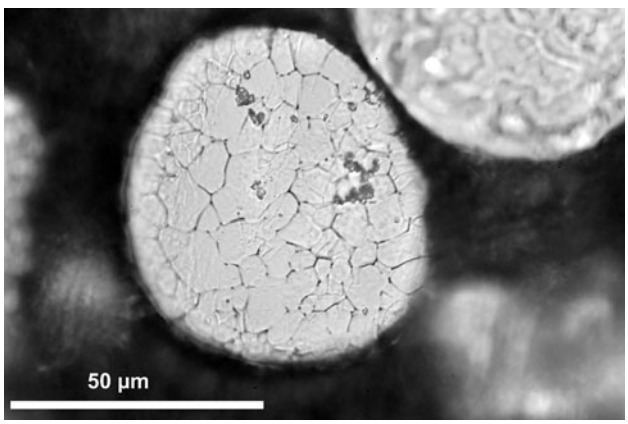

Fig. 4 Cross-section of an as-received powder particle after electrolytic etching

the fine-grained lamellae regions of the splats had average hardness values of 70 ± 2.2 HV ($n = 5$). The measurements are consistent with the inhomogeneous microstructures observed, with the higher values measured in the fine lamellae regions resulting from a combination of grain refinement and strain hardening. These results suggest that the overall hardness of the coating changed due to the severe plastic deformation induced during the actual coating process, and the microstructure of the initial powder had a secondary effect. One can observe from Fig. 3 that the coating consists of a significant fraction of fine-grained material in the lamellae.

Figure 6 shows TEM images of the microstructure across three of the lamella regions that had δ thickness values ranging from 1.0 to 1.9 μm, which compares well with the average of 1.2 μm measured optically. Each lamella region consisted of recrystallized grains with diameters of 100–500 nm. The fine-grained structures contained a mixture of grains less than 200 nm, which were free of dislocations, along with grains that were 200–500 nm, which had high dislocation densities (see Fig. 6b, c). It has been suggested that grain boundary-based deformation mechanisms may account for the microstructures observed in these regions [36]. The coarse grains in the upper portion of Fig. 6a have grain sizes which are more consistent with those observed in the interior of the splats (see Fig. 3). This suggests that large thermal and strain gradients occurred in the heavily deformed lamellae, with the transition between the lamellae and the grain structures in the bulk of the splats being extremely short as shown in Fig. 7a. Grains with dimensions as small as 20 × 50 nm could be observed at the centerline of some of the fine-grained bands, and were elongated in the direction of the lamellae (see Fig. 7b), which is consistent with deformation under a compressive load. In addition, the ultra-fine grains shown in Figs. 6 and 7 also show thick grain boundary extinction contours, which indicate a high level of internal stresses in and around the grain boundaries. This supports the notion that grain boundary sliding may have occurred in these regions, as suggested by other investigators [37, 38]. Trapped oxides, probably originating from the surface of the as-received powder, were also observed at the fine-grained regions corresponding to the particle interfaces, consistent with previous studies of cold-sprayed particle interfaces [16].

A limited number of studies have used TEM to characterize the fine grains produced at the splat interfaces in conjunction with the coarser grains in the interior of the particle (as shown in Fig. 6a) since the field of view is rather restricted. It is more convenient to examine the grain structures in these microstructural regions by electron backscattered diffraction. For example, Zou et al. [17] argued that the fine grains are produced by dynamic recrystallization, where an accumulation of dislocations

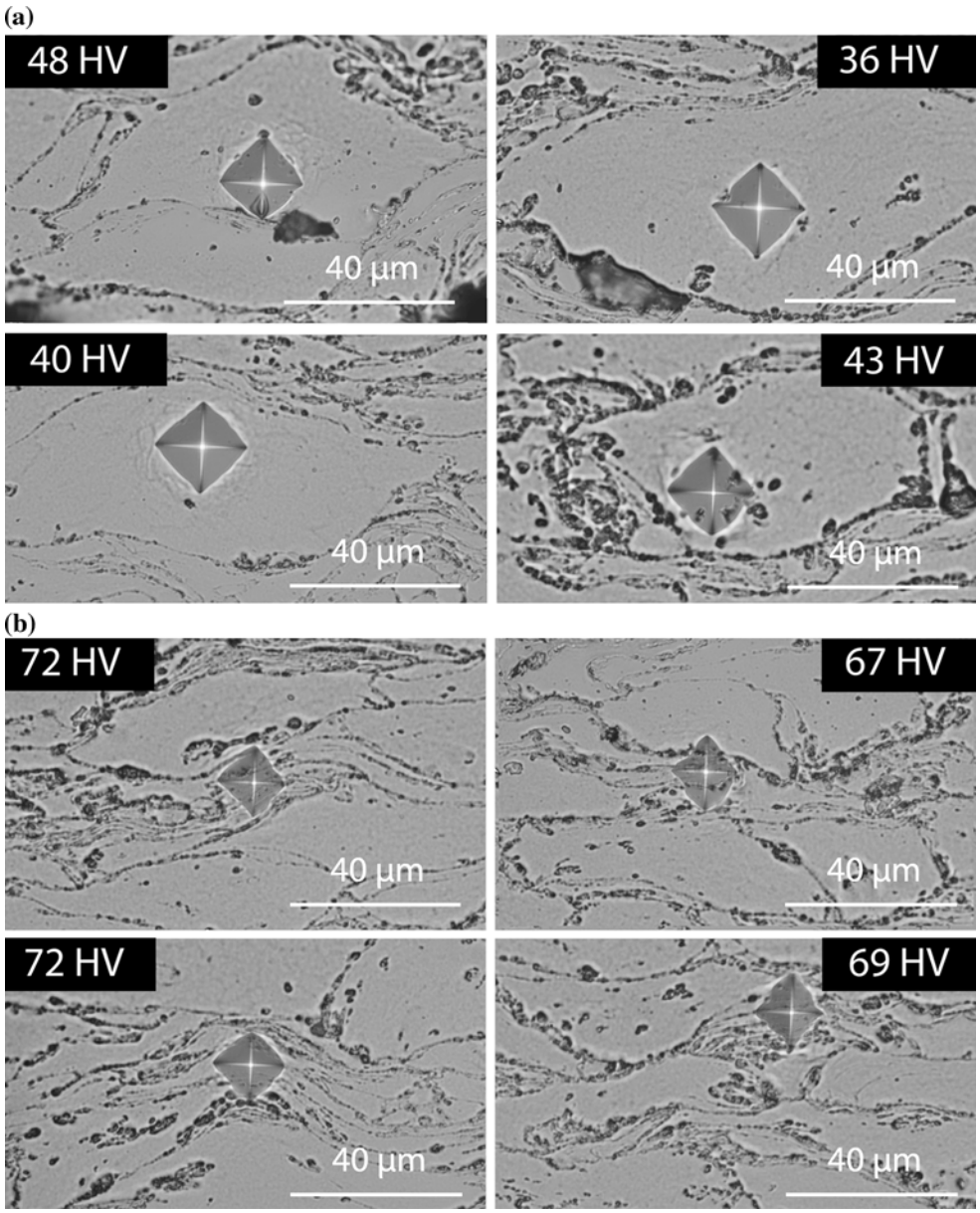

Fig. 5 Microhardness indentations and results for **a** the interior of particle splats and **b** the lamellae regions at particle interfaces

leads to the formation of elongated subgrains, with further deformation accommodated by lattice and subgrain rotation. The resulting microstructure leads to the formation of high angle grain boundaries, which is consistent with the selected area diffraction pattern observed in Fig. 6c.

Interfacial temperature estimates

All the terms required in Eq. 19 for the determination of the interface temperature between the splat and the substrate are known. Table 5 shows that the maximum interface temperature for 25 ± 8 μm aluminum particles deposited by low-pressure cold spraying is on the order approximately 400–745 °C, with particle velocities between 475 and 559 m/s. The table shows that for most of the particle diameters and velocities that were investigated in this study, the splat-substrate interface temperature was less than the melting point of aluminum (660 °C).

Figure 8 presents the variation of the non-dimensional splat–substrate interface temperature with the non-dimensional particle diameter. In dimensionless form, the interface temperature and droplet diameter are, respectively,

$$\theta = \frac{T_{\text{interface}} - T_{\text{g}}}{T_{\text{g}}} \text{ and } \xi = \frac{d_{\text{p}}}{D_{\text{nozzle}}}. \tag{20}$$

The chart also presents the curves as a function of the non-dimensional particle velocity, $V* = \frac{V_{\text{p}} L_x}{\alpha}$. It can be seen that as the particle diameter and velocity increases, the

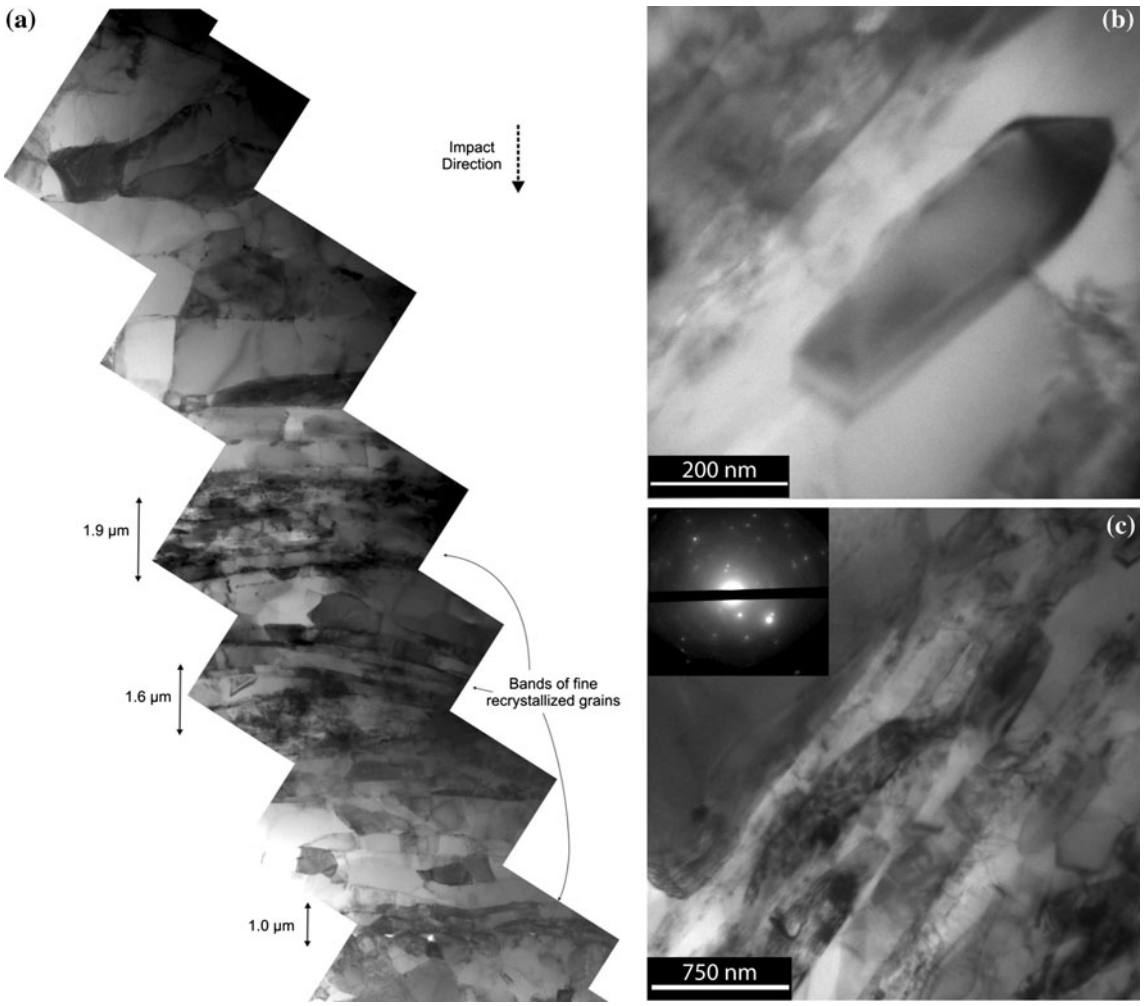

Fig. 6 **a** TEM montage of the bands of fine-grained structures observed in the cold-sprayed aluminum taken from a transverse section through the coating, **b** dislocation-free grain in the deformed band, and **c** grains with high dislocation density in the deformed band

interface temperature increases. As the mass and velocity of the particles increase, the kinetic energy also increases to provide additional energy for interfacial heating. The interface temperature is nearly constant when the particle velocity is low, which suggests that localized heating will not be observed for particles moving at lower velocities, irrespective of their diameter. As particle velocity increases, the interface temperature increases, and in these cases, shear band localization will be expected to be dominant. Given the non-dimensional nature of the parameters in Fig. 8, it could be applied to materials other than aluminum to estimate the splat-substrate interface temperatures.

The wide range of interface temperatures (see Table 5) confirms that the velocity of the incoming particles play a dominant role in interfacial heating and possibly melting at the interface. However, the model presented assumes that all particles in question are undergoing the same amount of strain. It is exceptionally difficult to quantify an accurate relationship between particle velocity and equivalent strain imposed during impact in order to determine conclusively the interfacial temperature. For example, a distribution of particle velocities and particle diameters will always be present in an actual coating, and the present study merely proposes a methodology for estimating the upper and lower limits of the interface temperature. Despite the inflated interfacial temperature range calculated, it can be concluded from the model presented that the actual interfacial temperatures were sufficient to promote dynamic recrystallization within the highly deformed bands of material between the particles, resulting in deformed grains with sizes as fine as 20–50 nm. For example, the recrystallization temperature of commercially pure aluminum is approximately 200 °C [39, 40], and previous work using molecular dynamics has predicted that the average grain size of aluminum deformed at comparable temperatures and strain rates was 20–29 nm [36].

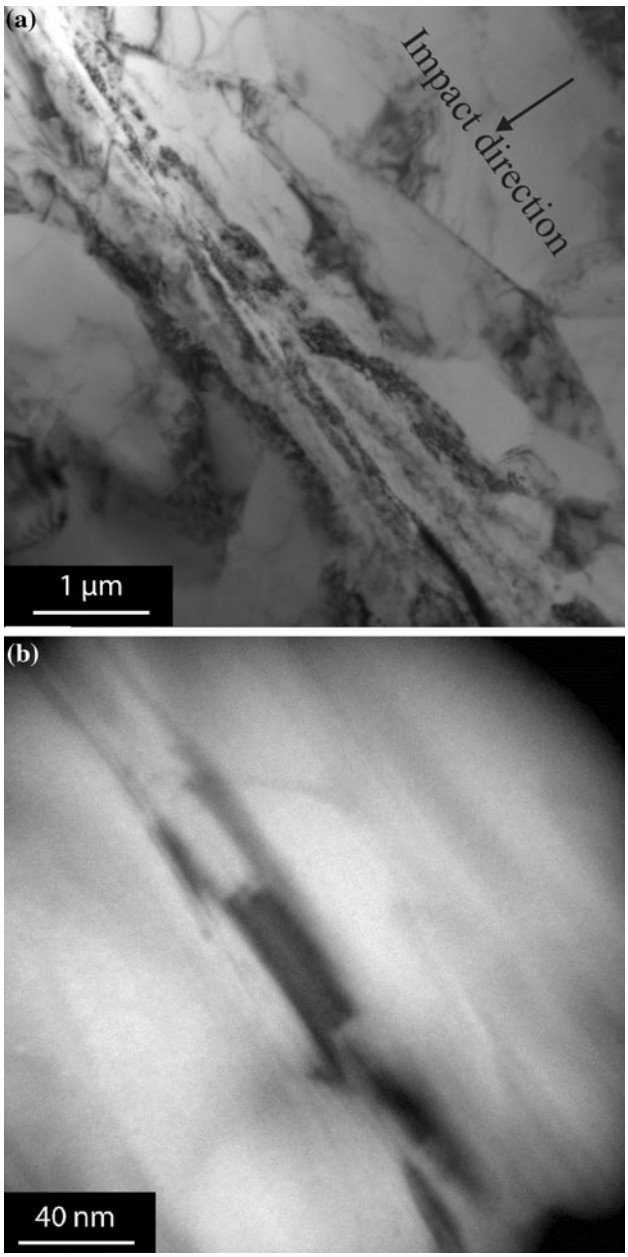

Fig. 7 **a** TEM micrograph of a fine-grained lamellae region between coarse grains in the bulk of the particle and **b** detail of a 20 by 50 nm grain at the centre of the lamella

Since the average grain size in the interior of the splat was comparable to that of the as-received powder, the assumption of localized heating and deformation within the lamellae region at the splat–substrate interface is supported. Only minor grain refinement is observed in the bulk of the particle, which is consistent with the relatively low equivalent strain value estimated for this region. This implies that the majority of the strain and heating is likely confined to the lamellae region at the splat–substrate interface.

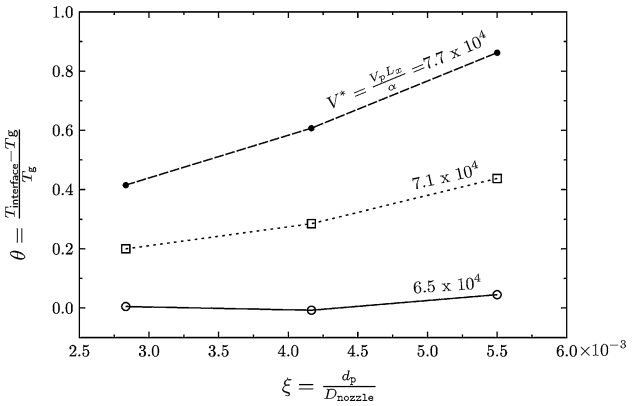

Fig. 8 Plot of non-dimensional splat–substrate interface temperature versus non-dimensional particle diameter

The increased hardness observed at the fine-grained lamellae produced at the interfacial regions are readily explained by the Hall–Petch relation. It is striking to note that the nanocrystalline grains observed in the lamellae regions could be retained at the temperatures calculated for the interface or bulk interior of the particle, since grain growth may occur in pure aluminum even at temperatures greater than 100 °C [39]. Despite the high temperatures produced, significant grain coarsening of the fine grains produced by the severe plastic deformation does not occur due to the highly transient nature of the impacts. This has implications on the feasibility of fabricating fully nanocrystalline bulk coatings from conventional polycrystalline powders using the cold spraying technique.

Although Hall et al. [19] have shown that nanocrystalline base materials can retain their microstructure during cold spraying, it may be possible to fabricate a microstructure which is comprised entirely of fine-grained lamellae material, provided that the particle size and initial velocity are appropriate. The hardness of the coating may be improved by increasing this fraction through the use of higher cold spray gas pressures, resulting in increased impact velocities and strain rates. However, it should be noted that the feasibility of generating a completely nanocrystalline structure in the final deposit is also limited by deposition efficiency, since erosion effects dominate at the highest velocities and cause the deposition rate to reach negative values, that is, resulting in removal of the previously deposited material [13]. Under these conditions the high velocities result in hydrodynamic penetration of the substrate, which has also been commonly associated with impact dynamics occurring in large scale projectiles [2].

The results of this study suggest that, for particles in low-pressure cold spraying, limited melting may occur at the interface for the majority of particles. However, melting may still be possible for particles that can achieve higher in-flight temperatures and velocities (see Table 5;

Fig. 8). Further, melting and metallurgical bonding may be more dominant in high-pressure, high-temperature cold spraying where pressures on the order of 400 psig (3 MPa gage) can generate significantly high particle velocities. It should not be assumed that melting is a strict prerequisite for joining to occur, since solid state bonding may occur even at room temperature if there is sufficient pressure to promote metallurgical bonding and the strain at the interface is sufficient to disrupt oxide layers [41]. These factors are highly dependent on the processing parameters, and this study has examined the influence of the kinetic energy on the temperature and microstructural gradients produced in the cold-sprayed coatings.

Conclusion

A simplified energy conservation model was coupled with microstructural analyses to estimate the temperature at the interface of deformed cold-sprayed particles and a substrate. An analysis of the deformed microstructures produced in cold-sprayed aluminum coatings indicated that a significant fraction of the particle deformation occurred within a localized lamellae region, about 1.2 μm in thickness at the interfaces between the splats. Optical micrographs indicated that particles with an average diameter of 25 μm underwent an average equivalent strain of 1.25. Characterization of the coating using optical and electron microscopy revealed a highly inhomogeneous microstructure, comprising splats with grain sizes around 6.5 μm on the interior, while the splat interface regions had grain sizes as fine as 20 nm. The results of an analytical model to determine the splat–substrate interface temperature suggested that the conservative maximum temperature at the interface, within the highly deformed lamella region, was on the order of 400–745 °C. These results indicate that extensive grain refinement at the interfaces between splats is directly controlled by the kinetic energy transfer to deformation energy and interfacial heating during impact, and that widespread local melting of the aluminum at the splat–substrate interface probably did not occur in low-pressure cold spraying.

Acknowledgements Funding for this project was provided by the Natural Sciences and Engineering Research Council of Canada (NSERC), the Government of Alberta Small Equipment Grants Program (SEGP), and the Canada Foundation for Innovation (CFI). The authors gratefully acknowledge the assistance of Dr. Eric Irissou with DPV-2000 measurements.

References

1. Alkhimov A, Kosarev V, Papyrin A (1990) Dokl Akad Nauk SSSR 315:1062
2. Schmidt T, Gärtner F, Assadi H, Kreye H (2006) Acta Mater 54:729
3. Klinkov S, Kosarev V, Rein M (2005) Aerosp Sci Technol 9:582
4. Grujicic M (2007) In: Champagne V (ed) Fundamentals of cold-gas dynamic spray. Woodhead Publishing Limited, London
5. Assadi H, Gartner F, Stoltenhoff T, Kreye H (2003) Acta Mater 51:4379
6. Papyrin A, Kosarev V, Klinkov S, Alkhimov A, Fomin V (2007) Cold spray technology. Elsevier, Amsterdam
7. Tokarev A (1996) Met Sci Heat Treat 38:136
8. Vlcek J, Gimeno L, Huber H, Lugscheider E (2003) In: International thermal spray conference 2003: advancing the science and applying the technology, Orlando
9. Zhang D, Shipway PH, McCartney DG (2003) In: International thermal spray conference 2003: advancing the science and applying the technology, Orlando
10. Li C-J, Li W-Y, Xi'an PRC, Fukanuma H, Saitama J (2004) In: International thermal spray conference 2004: advances in technology and application, Osaka
11. Vlcek J, Gimeno L, Huber H, Lugscheider E (2005) J Therm Spray Technol 14(1):125
12. Hussain T, McCartney D, Shipway P, Zhang D (2009) J Therm Spray Technol 18:364
13. Schmidt T, Assadi H, Gärtner F, Richter H, Stoltenhoff T, Kreye H, Klassen T (2009) J Therm Spray Technol 18:794
14. Barradas S, Guipont V, Molins R, Jeandin M, Arrigoni M, Boustie M, Bolis C, Berthe L, Ducos M (2007) J Therm Spray Technol 16:548
15. King P, Zahiri S, Jahedi M (2008) Acta Mater 56:5617
16. Borchers C, Gartner F, Stoltenhoff T, Kreye H (2004) J Appl Phys 96:4288
17. Zou Y, Qin W, Irissou E, Legoux J-G, Yue S, Szpunar J (2009) Scr Mater 61:899
18. Li C, Li W, Wang Y (2005) Surf Coat Technol 198:469
19. Hall A, Brewer L, Roemer T (2008) J Therm Spray Technol 17:352
20. Koch C (2007) Structural nanocrystalline materials: fundamentals and applications. Cambridge University Press, Cambridge
21. Ajdelsztajn L, Jodoin B, Kim G, Schoenung J (2005) Metall Mater Trans A 36A:657
22. Grujicic M, Zhao C, DeRosset W, Helfritch D (2004) Mater Des 25:681
23. Goldbaum D, Chromik R, Yue S, Irissou E, Legoux J-G (2011) J Therm Spray Technol 20:486
24. Borchers C, Gärtner F, Stoltenhoff T, Assadi H, Kreye H (2003) J Appl Phys 93:10064
25. Kapoor R, Nemat-Nasser S (1998) Mech Mater 27:1
26. Johnson G, Cook W (1983) In: 7th international symposium on ballistics, The Hague
27. Raybould D (1981) J Mater Sci 16:589. doi:10.1007/BF02402774
28. Jiji L (2009) Heat conduction, 3rd edn. Springer, Berlin
29. Shapiro A (1953) The dynamics and thermodynamics of compressible fluid flow, vol I. The Ronald Press Company, New York
30. Kaye J (1954) J Aeronaut Sci 21:117
31. Shapiro A (1954) The dynamics and thermodynamics of compressible fluid flow, vol II. The Ronald Press Company, New York
32. Dykhuizen R, Smith M (1998) J Therm Spray Technol 7:205
33. Legoux J-G, Irissou E, Moreau C (2007) J Therm Spray Technol 16:619
34. Akarca S, Song X, Altenhof W, Alpas A (2008) Proc Inst Mech Eng L 222:209
35. Boyer H, Gall T (1985) Metals Handbook, vol 2. ASM International, Materials Park
36. Gerlich A, Yue L, Mendez P, Zhang H (2010) Acta Mater 58:2176

37. Gerlich A, Shibayanagi T (2009) Scr Mater 60:236
38. Kaibyshev O (2000) Scientific bases, achievements and promises of superplastic deformation. Gilem, Ufa
39. Humphreys F, Hatherly M (2002) Recrystallization and related annealing phenomena. Pergamon Press, Oxford
40. Dimitrov O, Fromegeau R, Dimitrov C (1978) In: Haessner F (ed) Recrystallization of metallic materials. Dr. Riederer-verlag GmbH, Stuttgart
41. Lancaster J (1999) Metallurgy of welding. Abington Publishing, Cambridge